PAPER

Interfacial rheology insights: particle texture and Pickering foam stability

To cite this article: Nick Brown et al 2023 J. Phys.: Condens. Matter 35 384002

View the article online for updates and enhancements.

You may also like

- Particle-laden fluid/fluid interfaces: physico-chemical foundations
 Eduardo Guzmán, Irene Abelenda-Núñez, Armando Maestro et al.
- Experimental study on the foam performance and fire extinguishing performance of aqueous foam stabilized by alkyl polyglucoside and urea
 Fan Li, Xiaoyang Yu and Ruowen Zong
- On the effectiveness of incorporating shear thickening fluid with fumed silica particles in hip protectors A Haris, B W Y Goh, T E Tay et al.

Interfacial rheology insights: particle texture and Pickering foam stability

Nick Brown, Alec de la Pena and Sepideh Razavi*

School of Chemical, Biological, and Materials Engineering, University of Oklahoma, 100 E. Boyd Street, Norman, OK 73019, United States of America

E-mail: srazavi@ou.edu

Received 3 March 2023, revised 31 May 2023 Accepted for publication 13 June 2023 Published 23 June 2023



Abstract

Interfacial rheology studies were conducted to establish a connection between the rheological characteristics of particle-laden interfaces and the stability of Pickering foams. The behavior of foams stabilized with fumed and spherical colloidal silica particles was investigated, focusing on foam properties such as bubble microstructure and liquid content. Compared to a sodium dodecyl sulfate-stabilized foam, Pickering foams exhibited a notable reduction in bubble coarsening. Drop shape tensiometry measurements on particle-coated interfaces indicated that the Gibbs stability criterion was satisfied for both particle types at various surface coverages, supporting the observed arrested bubble coarsening in particle-stabilized foams. However, although the overall foam height was similar for both particle types, foams stabilized with fumed silica particles demonstrated a higher resistance to liquid drainage. This difference was attributed to the higher yield strain of interfacial networks formed by fumed silica particles, as compared to those formed by spherical colloidal particles at similar surface pressures. Our findings highlight that while both particles can generate long-lasting foams, the resulting Pickering foams may exhibit variations in microstructure, liquid content, and resistance to destabilization mechanisms, stemming from the respective interfacial rheological properties in each case.

Supplementary material for this article is available online

Keywords: particle-laden interfaces, Pickering foams, interfacial rheology

(Some figures may appear in colour only in the online journal)

1. Introduction

Particle-stabilized (i.e. Pickering) foams have shown applicability in various areas ranging from froth flotation of minerals [1, 2] and decontamination of nuclear facilities [3, 4] to tissue scaffolding [5, 6] and drug delivery [7–10]. Foams are promising candidates for applications in the petroleum industry including enhanced oil recovery [11–13], hydraulic fracking of unconventional oil and gas resources [14, 15] and gas well deliquification [16], because their low liquid

content causes less damage in water sensitive formations and reduces the water consumption and disposal in subsurface resource recovery applications. The wide applicability range of Pickering foams stems from their ability to withstand destabilization mechanisms such as coalescence [17, 18] and Ostwald ripening [19–21], and to remain stable under high temperature [22, 23] and high salinity [24–26] conditions compared to surfactant-stabilized foams [27–29]. The enhanced stability arises in part from the large desorption energy of particles from a fluid-fluid interface that is dependent on the particle size and its position at the interface. For instance, a particle with nominal size of 250 nm and of neutral wettability (i.e. $\theta = 90^{\circ}$) possesses an interfacial binding energy of

^{*} Author to whom any correspondence should be addressed.

 $\sim \! 10^6~k_{\rm B}T$, where $k_{\rm B}$ is the Boltzmann's constant and $k_{\rm B}T$ is the thermal energy. Therefore, due to their large desorption, in comparison to the thermal energy, particles can irreversibly adsorb onto a fluid–fluid interface, unlike surfactants which can be reversibly exchanged between the interface and the bulk solution.

A number of key particle attributes are reported to impact the stability and properties of Pickering foams. Adding particles to foams in specific concentrations has been shown to improve the foam half-life and foam volume compared to those formed solely by foaming agents like surfactants [30–35]. For example, Tyowua and Binks [32] showed that for an air-water system, increasing the concentration of particles (6 μ m hollow Expancel[®] microplastic particles), in the range of 0.5–10 wt.%, caused the average bubble radius to initially increase from 100 μ m to 350 μ m and subsequently remain stable at around 200 μ m with 10 wt.% particles in the system. This trend was attributed to low bubble stability against coalescence in foams prepared with lower particle concentrations that resulted in partial surface coverage of bubbles by the particles, whereas increasing the particle coating on the bubble surface using a higher concentration of particles led to bubbles sizes that remained uniform after generation. Increasing the particle concentration not only altered the microstructure of the foam, but it also extended its half-life tremendously leading to foams lasting upwards of six months for all particle concentrations tested.

Particle size is another attribute that is reported to impact 'foaminess', i.e. the volume percent of air incorporated into the system, as shown by Bindal *et al* [36]. It was reported that by increasing the particle size, at 10 wt.% particle concentration, the overall foaminess decreased from 550% for the 8 nm particles to only around 20% for 100 nm particles. The reduction in foaminess with the use of bigger particles was attributed to their lower effective volume fraction within the lamellae, as well as a decrease in the number of particle layers that can form in the foam lamellae, which plays a role in the stability of the liquid film against drainage.

Surface wettability of particles is also shown to impact the stability of Pickering foams; not only can it affect the interfacial binding energy of the particles but also the type and strength of interparticle interactions present between the interfacially bound particles [37–39]. Altering the particle contact angle at the interface affects the area of contact between the two fluid phases and changes the binding energy of the particle to the fluid interface. Particles that remove the largest possible area from the air-water interface, i.e. $\theta \sim 90^{\circ}$, have shown to produce larger foam volumes and longer-lasting foams [37, 40-42], while those of extreme wettability, i.e. very hydrophilic ($\theta < 30^{\circ}$) or very hydrophobic ($\theta > 150^{\circ}$) particles, tend to be poor foam stabilizers [43]. Taking the maximum capillary pressure of the foam lamellae into account, it has been shown that the contact angle corresponding to most stable configuration is $\sim 86^{\circ}$ for the case with a double particle layer within the lamellae and $\sim 71^{\circ}$ for a single particle layer [44]. Worthen et al [41] used hydrophobically modified fumed silica nanoparticles and reported that decreasing the number of silanol (i.e. SiOH) groups on the silica particle surface, thus increasing the particle contact angle at the air—water interface, led to the generation of foams with a higher initial volume. In particular, the foam height increased from ~ 0.65 cm to ~ 2.3 cm using hydrophobically modified particles with 70% SiOH and 35% SiOH surface groups, respectively.

Particle anisotropy, in surface or shape, can also impact the binding strength and resulting interparticle interactions at a fluid interface [45–48]. Ozdemir et al [49] studied how particle shape anisotropy can lead to varied foam characteristics using spherical silica nanoparticles (\sim 11 μ m) and needlelike sepiolite particle (\sim 45 μ m). By increasing the particle concentration from 0.01 to 2 wt.%, the overall foam volume increased from 50 ml to 70 ml for those stabilized with spherical particles, whereas the needle-like particles imparted a more pronounced impact on the foam volume and increased it from 100 ml to 180 ml. The foams stabilized with 2 wt.% of the needle-like particles also exhibited an increased halflife time (1800 s) compared to their analogue stabilized with spherical particles (500 s). The improved foam stability in the case of needle-like particles was attributed to their ability to form a stronger interfacial network in contrast with the spherical particles.

The effect of other ingredients present in the solution, such as electrolyte [23, 25, 50, 51], surfactant [52–55], and polymer [56–59], on the stability of Pickering foams has also been studied in the literature [60, 61]. For example, Kostakis *et al* [62] found that increasing the electrolyte concentration, from 0.5 to 3 mM, in suspensions of fumed silica particles (20 nm) used in the generation of Pickering foams resulted in more stable bubbles and an enhancement in the bulk dynamic storage modulus of the foam system (from \sim 2 Pa to \sim 8 Pa). The reduction in Debye length at higher electrolyte concentrations, enables the formation of a more tightly packed particle network on the bubble surface, which can enhance the foam stability via resistance to bubble coarsening as well as the increased viscosity.

While the impact of various particle attributes on the bulk properties of Pickering foams has been extensively studied in the literature, examples of which are provided above, understanding the impact of particles on the resulting mechanical properties of a fluid-fluid interface is a growing field of research [63–71]. The interfacial rheological measurements, which are conducted by either expanding and contracting the interface (i.e. dilational mode) or changing the shape of the interface while keeping the interfacial area constant (i.e. shear mode) [72], provide insight on important attributes of particleladen interfaces. An example of such interfacial characteristic is the yield point of the particle network beyond which the interfacial microstructure breaks down in response to the applied stresses and the material begins to flow [50, 73–75]. Interfacial rheology can thus be employed in characterizing the ability of an interface to resist distortion and deformation, key factors when attempting to control the thin film drainage and retard or arrest bubble coarsening in foams [76, 77]. For instance, Zhu et al [78] studied the dilational rheological properties of interfaces in presence of hydrophilic anionic sulfonate-modified nanoparticles (28.5 \pm 0.2 nm) in tandem with the cationic surfactant Arquad 12–50 using pendant drop tensiometry. It was shown that while the surfactant-laden gas-liquid interface exhibited a negligible storage dilatational modulus $\kappa^{s\prime} \sim 0$ –10 mN m⁻¹, for surfactant concentration of 0.01-0.1 wt.%, the addition of 0.1 wt.% particles to the droplet containing 0.01 wt.% surfactant led to an enhancement in the modulus, $\kappa^{s\prime} \sim 20 \text{ mN m}^{-1}$. As the concentration of particles was further increased to 0.3 wt.%, the dilatational modulus reached $\kappa^{s\prime} \sim 70~\text{mN m}^{-1}$ indicating a more elastic interfacial network, which resulted in ultra-stable foams. To highlight the importance of interfacial shear properties and its connection to the bubble dissolution, Beltramo et al [19] studied interfacial networks of polystyrene spheres (~820 nm) and ellipsoids (\sim 2.48 μ m long and 0.45 μ m wide) formed at various surface coverages. It was found that with an increase in the particle surface packing, the yield stress of the network increased, and a higher pressure was necessary for the diffusion of gas through the interface, which highlights the link between interfacial properties and Ostwald ripening in foams.

Probing the rheological characteristics of an interface is thus pertinent to understanding the connections between particle impacts on the mechanical stability of a fluid-fluid interface and stability of Pickering foams. While a body of research exist on how changing the particle attributes alters the interparticle interactions and the mechanical properties of the resulting particle-laden interface, such as its elasticity and collapse modes under applied stresses [74, 79, 80], less is known on the roles such interfacial characteristics play in the ensuing foam stability. The present study focuses on Pickering foams stabilized with fumed and spherical colloidal silica particles to not only elucidate the impact of particle surface area and roughness on the properties of the resulting foam but also explain the differences observed between the two systems from the standpoint of interfacial rheology. Our findings highlight that the interfacial rheology of bubbles can be tuned by altering the roughness of particles present on their surface, and that rheological studies can be exploited in interfacial engineering of Pickering foams with a desirable set of properties.

2. Materials and methods

2.1. Silica particles

Hydrophobically modified spherical colloidal silica particles (250 nm nominal diameter, Fiber Optic Center Inc.) and fumed silica particles (TS-622, CAB-O-SIL®, Cabot Corporation) were utilized in all the experiments carried out under the current study. Scanning electron microscopy (NEON Field-Emission SEM, Zeiss) images of both particle types are provided in figure 1. The fumed silica particles were made up of primary silica nanoparticles with diameter of 28 \pm 5 nm determined via SEM measurements. Using the dynamic light scattering (Brookhaven Instruments, NanoBrook Omni DLS) technique, the hydrodynamic diameter $(D_{\rm H})$ of the fumed particles, dispersed in water, through an ethanol solvent exchange step, was measured to be 196 ± 70 nm. Fumed silica particles possessed a surface area of $195 \pm 20 \text{ m}^2 \text{ g}^{-1}$, while the surface area of the spherical colloidal particles was calculated to be 9 m 2 g $^{-1}$.

2.2. Surface wettability

Silica particles exhibit a hydrophilic character when dispersed in water due to the dissociation of their surface silanol groups. To promote their binding to the air-water interface, both particle types were hydrophobically modified with dimethyldichlorosilane (DMDCS, Sigma Aldrich). The fumed silica particles were treated with DMDCS by the manufacturer and were used as received. From the zeta potential measurements, it was determined that the fumed silica particles were negatively charged with a zeta potential value of -26 ± 1 mV. Spherical colloidal particles were rendered hydrophobic using DMDCS following a procedure established in the literature [81]. Untreated spherical colloidal particles had a zeta potential of -52 ± 2 mV, while the hydrophobic modification reduced the magnitude of their zeta potential to -31 ± 2 mV. Both the fumed and spherical silica particles had moderately negative zeta potentials (i.e. larger than 25 mV in magnitude), which can aid in their colloidal stability in the solution. Anhydrous ethanol, chloroform, and cyclohexane, purchased from Fischer Scientific, were utilized in sample preparation and silanization. Ultrapure deionized water (18.2 M Ω cm) used throughout the study was generated via Milli-Q[®] IQ 7000 Ultrapure Lab Water System (Millipore Sigma).

Wettability of particles were estimated by measuring the contact angle of a water droplet on glass substrates coated with each particle type; the particle networks were formed on the substrate using particle dispersions in ethanol via convective assembly technique following the procedure by Prevo and Velev [82]. A water droplet was then placed on the particle coated substrates and the contact angle was determined using a tensiometer (Attension Theta, Biolin Scientific) by fitting the droplet shape, examples of which are provided in figure 2. The monolayer of spherical particles was found to yield a water contact angle of $126 \pm 11^{\circ}$, while for the monolayer of fumed silica particles the water contact angle was measured to be $140 \pm 3^{\circ}$. The larger contact angle obtained for the fumed silica particles could be attributed to their larger surface area and the impact of roughness on enhancing the resulting wettability of a surface [83].

2.3. Foam characterization

Pickering foam samples were generated and analyzed using the dynamic foam analyzer DFA100 (Krüss Scientific) by sparging the particle dispersions. To set up the prism column, which holds the particle dispersion and the resulting foam, a sealing ring was inserted on the bottom of the cylinder, followed by a filter plate, and a secondary sealing ring. The filter plate used had a pore size of 16–40 μ m. The prepared particle dispersion (see supporting information) was added into the prism column of the DFA100 and sparged at 0.2 1 min⁻¹ air flow rate for 30 s to generate the Pickering foams. To compare the characteristics of Pickering foams stabilized by silica particles with widely used foaming agents, sodium dodecyl sulfate (SDS) (Sigma Aldrich) solution was also used at 0.12 wt.% to generate foams in this study. A video of foam

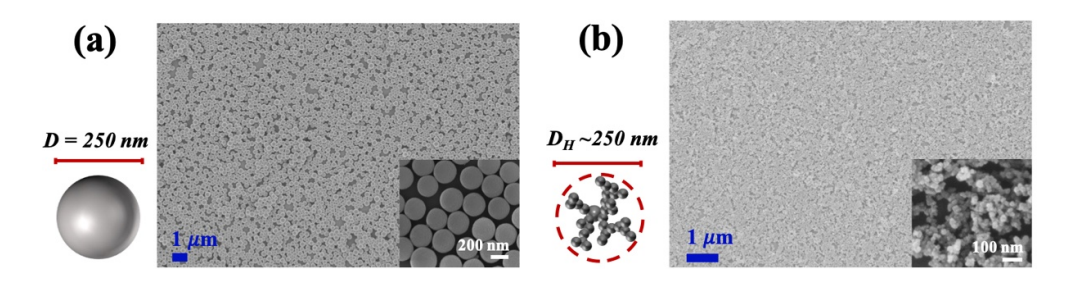


Figure 1. Scanning electron microscopy images of (a) fumed silica particles and (b) spherical silica particles.



Figure 2. Contact angle of a water droplet on glass substrates coated with a monolayer of hydrophobically modified (a) spherical silica particles and (b) fumed silica particles.

generation and detailed information on DFA100 specifics and modules are provided in the supporting information.

The dynamic foam analyzer (DFA100) is equipped with a foam structure module accompanied by a camera that utilizes the prism attachment of the column to generate images of the foam microstructure (see figures S1(a) and (b)). The DFA100 is also equipped with a liquid content module (LCM) that measures the resistance across the foam at various heights (see figures S1(c) and (d)). Using the LCM, the conductivity, which is the inverse of resistance, is measured at each sensor location and is linked to the volume fraction of the continuous phase (ϕ) at that sensor height: [84]

$$\phi = \frac{3\sigma(1+11\sigma)}{1+25\sigma+10\sigma^2} \tag{1}$$

where σ is the relative conductivity defined as $\sigma_{sample}/\sigma_{liquid}$ and σ_{sample} is the conductivity being measured at each sensor location along the column, while σ_{liquid} is the conductivity of the solution measured by the reference sensor. The volume fraction of the continuous phase (ϕ) can then be used to calculate the osmotic pressure (Π_{OSM}) across the foam column as follows: [85]

$$\Pi_{\text{OSM}} = K \frac{\gamma}{R_{32}} \frac{(\phi_{\text{c}} - \phi)^2}{\sqrt{\phi}} \tag{2}$$

 γ is the interfacial tension, R_{32} is the Sauter mean radius of the bubbles, and ϕ_c is the critical volume fraction of the continuous phase below which jamming of the bubbles takes place. It is shown that ϕ_c depend on the polydispersity of the bubbles and is equal to 0.26 or 0.36 for a monodisperse or polydisperse system, respectively [86]. K is a constant associated with the polydispersity of the system, with values of 7.3 and 3.2 for foams composed of monodisperse and polydisperse bubbles, respectively [86, 87]. Based on the foam microstructure information obtained in our foam systems, the

values of ϕ_c and K corresponding to polydisperse foams are used for all the calculations carried out in the present study. Normalizing the osmotic pressure with γ/R_{32} yields a reduced osmotic pressure $\bar{\Pi}_{OSM}$, which allows for comparison of the liquid drainage across foam samples stabilized by different species. From equation (2), it can be seen that $\bar{\Pi}_{OSM}$ is proportional to $\phi^{-1/2}$; as the volume fraction of the continuous phase present in the lamellae decreases via liquid drainage, the reduced osmotic pressure will increase over time. It should be noted that if the value of the continuous phase volume fraction, calculated from the LCM data, was found to be larger than the critical volume fraction (i.e. $\phi > 0.36$), the osmotic pressure would be set to zero.

2.4. Drop shape tensiometry

The dilational rheological behavior of particle-laden interfaces was probed using a tensiometer (Theta Lite, Biolin Scientific). Details on the preparation of particle-laden drops are provided in the supporting information. The effective surface tension in presence of particles can be calculated by fitting the drop shape to the Young—Laplace equation as follows:

$$\gamma_{\text{eff}} = \frac{\Delta P g R_0}{\beta} \tag{3}$$

where ΔP is the Laplace pressure, g is the standard gravity, R_0 is the droplet radius of curvature, and β is the shape factor of the droplet being fitted. To carry out tensiometry measurements, the droplet volume was reduced from its initial value, i.e. $20~\mu l$ for the 14—gauge needle, at a rate of $20~\mu l$ min⁻¹, to achieve higher surface pressures ($\Pi_{\rm SP}$) by increasing the particles surface coverage. Surface pressure ($\Pi_{\rm SP}$) is defined as the difference between the air—water surface tension ($\gamma_{\rm aw}$) and the effective surface tension in presence of particles ($\gamma_{\rm eff}$). Once the surface pressure of interest was reached, in the range of 0–40 mN m⁻¹, the droplet was pulsated, within the linear

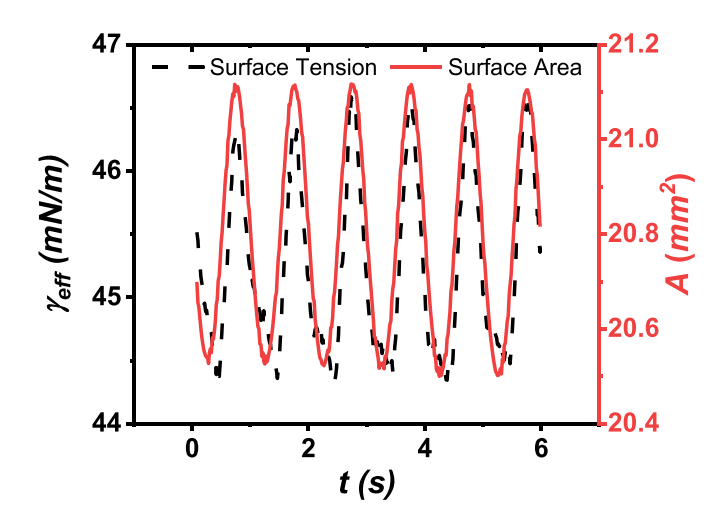


Figure 3. Oscillation of the surface area (A) and the resulting change in the effective surface tension $(\gamma_{\rm eff})$, with a phase angle (δ) . Data was obtained by oscillating a spherical colloidal particle-laden air—water interface.

viscoelastic regime (LVR), and the resulting response in the effective surface tension was tracked, as depicted in figure 3. The oscillations were carried out at 1 Hz for six cycles followed by 0.1 Hz, with a maximum volume change of $\pm 0.2~\mu l$ (i.e. total volume change of 0.4 μl per cycle), which corresponded to area strain amplitudes in the range of 0.85–1.76% throughout the studied surface pressures. The applied changes to the surface area, along with the accompanying effective surface tension results, were then used to determine the complex dilational surface modulus as follows:

$$\kappa^{s*} = \frac{\partial \gamma(t)}{\partial \ln A(t)}.$$
 (4)

The elastic $(\kappa^{s'})$ and viscous $(\kappa^{s''})$ components of the dilational modulus can be calculated by:

$$\kappa^{s\prime} = |\kappa^{s*}| \cos \delta \tag{5a}$$

$$\kappa^{s\prime\prime} = |\kappa^{s*}| \sin \delta \tag{5b}$$

where phase angle, δ , is the angular displacement between the applied oscillations in the surface area (A) and the response of particle-laden interface in form of change in the effective surface tension ($\gamma_{\rm eff}$), as illustrated in figure 3. After the completion of oscillatory measurements at one surface pressure, the drop was compressed again to reach the next surface pressure of interest at which point the oscillatory measurements were carried out. This process was repeated to cover data acquisition on particle networks exhibiting surface pressures in the range of 0–40 mN m⁻¹.

In order to assess the accuracy of data obtained from the tensiometry measurements, the magnitude of Worthington number was calculated at experimental settings used in all the measurements as follows [88]:

$$Wo = \frac{\Delta \rho V_{\rm d}}{\pi D_n \gamma_{\rm eff}} \tag{6}$$

where $\Delta \rho$ is the difference in density of the two phases, in this case air and water, $V_{\rm d}$ is the volume of the drop under study, and $D_{\rm n}$ is the outer diameter of the needle used. Since the density difference, gravity, and the needle diameter are all constants, Worthington number is solely a function of the drop volume and the effective surface tension. It provides a measure for the magnitude of the gravitational force in comparison to that of the capillary force and varies in the range from 0 to 1, where data obtained from experimental measurements with Wo>0.25 were deemed useful [89]. The phase angle (δ) was also used to analyze the validity of the data sets, as viscoelastic samples should exhibit phase angles in the range of $0^{\circ} < \delta < 90^{\circ}$ and the data points with $\delta > 90^{\circ}$ pointed at a collapsed monolayer.

2.5. Interfacial shear rheology

To examine the shear response of monolayers at different particle surface coverages, we have integrated a ribbon trough (Biolin Scientific) with a custom designed double wall ring (DWR) geometry [75] on a DHR2 stress-controlled rheometer (TA instruments) following the work of Vermant and coworkers (see figure S2) [90, 91]. Details on the specifics of the setup and preparation of the particle-laden interfaces, at various surface pressures in the range of 0–40 mN m⁻¹, are provided in the supporting information. The amplitude sweep experiments were conducted at 1 Hz, over shear strains in the range of 0.001%–100%, to determine the LVR for the particle-laden interfaces and their corresponding yield strain. The frequency sweeps were conducted within the LVR, at 0.05% strain, over a frequency range of 0.1–10 rad s⁻¹.

3. Results & discussion

3.1. Overall foam stability

The initial screening of foams involved the investigation of total sample height and how it altered when different particle types were used to stabilize the bubbles; samples of SDSstabilized foams were also examined for comparison. The total height H_t (foam + solution) of foam samples, averaged over three trials, are shown in figure 4(a). The initial total heights, H_{t0} , obtained right after sparging, are similar for the three stabilizers used in this study and are as follows; 134 ± 2 mm, 138 ± 4 mm, and 129 ± 7 mm for foams generated with SDS molecules, fumed particles, and spherical colloidal particles, respectively. These values were used to normalize the data and compare the changes in the total height with time across various stabilizers. As shown in figure 4(b), there is a noticeable decrease in the normalized total height (H_t/H_{t0}) for the surfactant-stabilized sample over an hour. Pickering foams maintained a relatively constant height over the same time span, which highlighted their ability to resist destabilization processes. To further investigate the effectiveness of the stabilizers, we examined the change in the foam height (H_f) and solution height (H_s) separately, as shown in figures 4(c) and (d), respectively. The SDS-stabilized system exhibited $\sim 50\%$ decrease in its foam height over an hour, which is accompanied

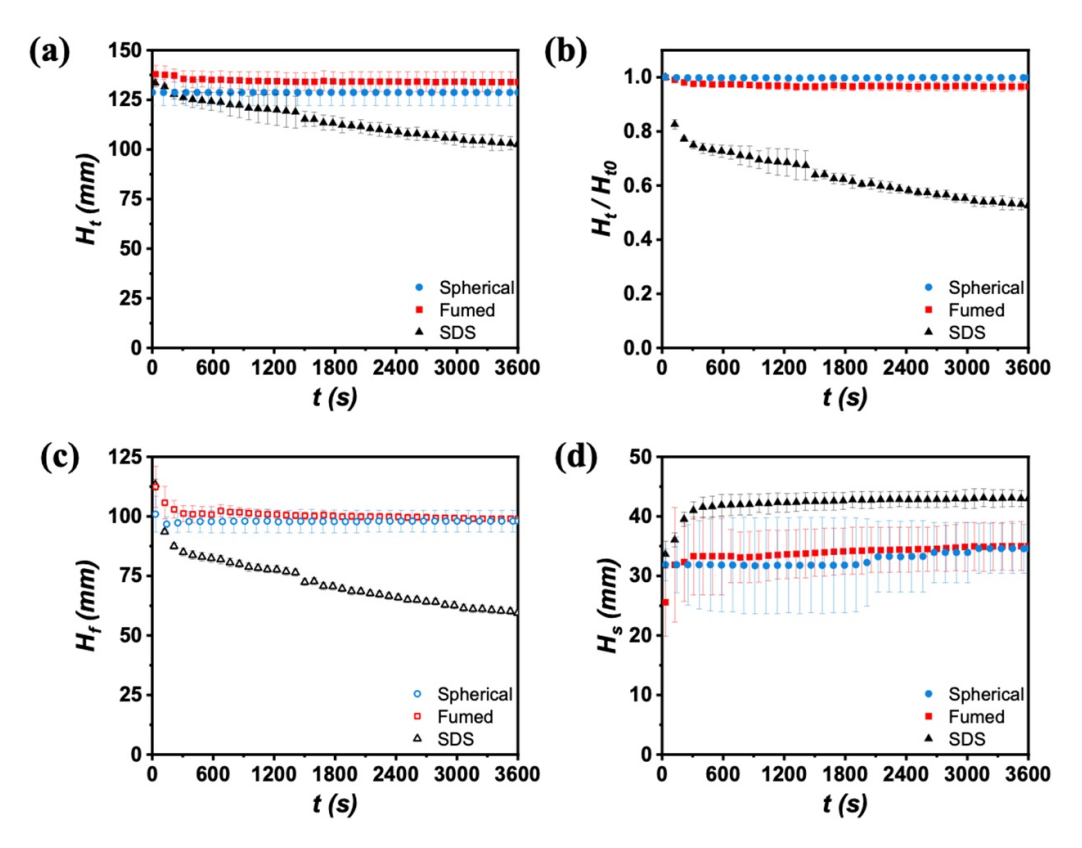


Figure 4. (a) Total height H_t (foam + solution) for foam systems stabilized with spherical silica particles (blue circles), fumed silica particles (red squares), and SDS molecules (black triangles); (b) normalized height (H_t/H_{t0}) , (c) foam height H_f , and (d) solution height H_s for the same systems shown in (a); the concentration of stabilizers in the dispersion used for foam generation is as follows: 6.0 wt.% spherical colloidal silica particles, 2.0 wt.% fumed silica particles, and 0.12 wt.% SDS surfactant molecules.

by doubling the drained solution height at the bottom of the column. In comparison, slower increase in solution height was observed for spherical particle-stabilized foams compared to the SDS system, whereas the fumed particle-stabilized foams exhibited the least drainage over an hour among the three systems studied. The enhanced stability of bubbles can be attributed to the strong binding energy of particles to the interface as well as the superior mechanical properties of particle networks formed at the interface armoring the bubble and arresting coarsening [18, 19, 92]. To further investigate the impacts of fumed and spherical particles on foam stability, we studied the osmotic pressure developed in these foam systems as a function of time as detailed in the next section.

3.2. Osmotic pressure

Once the foam is generated, initially the bubbles are spherical and loosely packed, the volume fraction of the continuous phase (ϕ) is larger than a critical value (ϕ_c) , and the packing of the dispersed bubbles cannot sustain a static stress (see figure 6(a), panel I for the case of SDS-stabilized foam). As the liquid drainage from the lamella takes place over time, under the influence of the gravitational field, the volume fraction of the dispersed bubbles increases in the foam (see figure 6(a), panel II). Drop in the value of the continuous phase volume fraction to below a critical value (ϕ_c) , leads to jamming of the bubbles and emergence of a network with a solid-like

response. Under these conditions, the appearance of static contact forces among the bubbles results in their polyhedral deformation, which is accompanied with an effective increase in the interfacial area and interfacial energy (see figure 6(a), panel III). Since the state with spherical bubble shape is the minimum interfacial energy state, when the bubbles become polyhedral, an osmotic pressure (Π_{OSM}) develops in the system to regain the sphericity by flowing the continuous phase back in between the jammed bubbles. The mechanical equilibrium established in the foam column under the gravitational field is due to the balance between the buoyancy force on the gas bubbles and the osmotic pressure [86]. As a result, studying the development of the osmotic pressure in a foam column can inform us on the liquid drainage that is taking place over time and the impact different stabilizers could have on providing stability against drainage. Using the LCM, which measure the resistance across the foam that lies between two sensors, volume fraction of the continuous phase can be calculated, at various heights throughout the foam column, and as a function of time. This analysis can be employed in investigating the liquid drainage across the foam height, which is then used to evaluate the change in the osmotic pressure over time and as a function of the stabilizer used in the system as detailed

The change in the reduced osmotic pressure of the foam samples under study are shown in figure 5 and as a function of sensor height within the foam, where the position of each

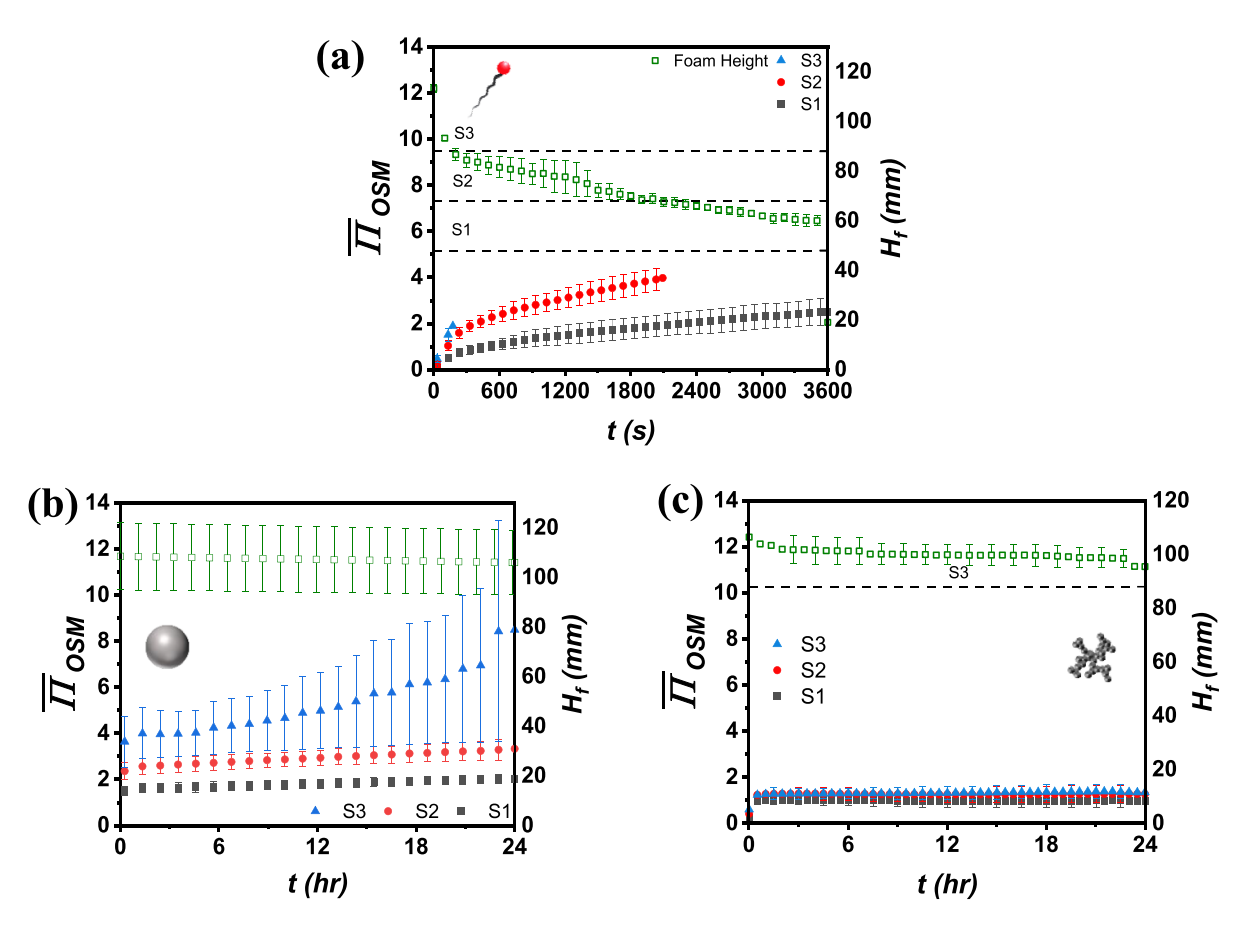


Figure 5. Reduced osmotic pressure versus time as a function of the sensor height: sensor 1 (S1, solid squares), sensor 2 (S2, solid circles), and sensor 3 (S3, solid triangles) are the sensors in touch with the foam sample and numbered from the bottom to top of the foam column. The change in the total foam height with time is also provided on each plot (open squares). Data is taken from foams stabilized with (a) 0.12 wt.% SDS molecules (b) 6.0 wt.% spherical silica particles, and (c) 2.0 wt.% fumed silica particles.

sensor is marked on the plot as well. Data on the change in the foam height over the same time frame is also provided. As can be seen in figure 5(a), there is a clear stratification of the reduced osmotic pressure as a function of height within the column in SDS-stabilized foam system; for example, after 1200 s has elapsed, the reduced osmotic pressure increased to $\Pi_{\rm OSM} = 1.5$ at position 48 mm within the column (i.e. sensor 1 location), while it reached $\Pi_{OSM} = 3.2$ at position 68 mm (i.e. sensor 2 location) as a result of liquid drainage that is occurring from the top to the bottom of the foam column. At all three-sensors positions, the reduced osmotic pressure also continuously increased over time for SDS-stabilized foam showing that the surfactant had negligible impact on stabilizing the foam against liquid drainage. For the spherical colloidal particle samples shown in figure 5(b), there is a clear stratification of the reduced osmotic pressure with time, measured at three locations in the foam, whereas for Pickering foam stabilized with fumed silica particles, the reduced osmotic pressure values plateaued with time, as shown in figure 5(c). In addition, for the latter case, values of reduced osmotic pressure are similar at all sensor heights within the foam. This result could be attributed to the presence of fumed silica particles on the interface and their impact on the bubblescale interfacial rheology, which sets the boundary conditions for the local fluid flow and is known to play a critical role in the liquid film drainage [44, 93]. Not only the reduced osmotic pressure remained fairly constant at a given height, there was no gradual change in the reduced osmotic pressure as a function of foam height and the values calculated from all three sensor were similar (see figure 5(c)). This result indicates that gravity-assisted liquid drainage was halted in the entirety of the foam to a large degree and that the foam wetness was uniform throughout the column for Pickering foams stabilized with fumed silica particles. Unlike the case of fumed silica particles, the foam stabilized with spherical particles had a larger reduced osmotic pressure when compared at the same time stamp; for example, after 24 h had elapsed, $\bar{\Pi}_{OSM} = 8.5 \pm 4.8$ for spherical particle sample, while $\Pi_{\rm OSM} = 1.3 \pm 0.3$ for fumed particles at position 88 mm within the column (i.e. sensor 3 location),. Because Π_{OSM} is inversely proportional to $\phi^{1/2}$, the obtained data indicates that when compared at the same foam height, the foam stabilized with spherical silica particles was drier, i.e. had a higher quality, than that stabilized with the fumed silica particles. The spherical colloidal foam itself was also stable against liquid drainage shown by the low slope of the reduced osmotic pressure (see sensor 1 data in all three cases). It was found that particles in general created foams that were more resistant to liquid drainage than the case of SDS-stabilized sample; in agreement with the data obtained on the change in the liquid height for the three systems, shown in figure 4(d).

In comparing the properties of the two Pickering foams under study, the spherical silica particle-stabilized foams had a larger gradient in reduced osmotic pressure across the foam column as well as a larger difference in foam quality as a function of height. This can be attributed to the large surface area of the particles in the latter case. The spherical colloidal particles had a lower surface area ($\sim 9 \text{ m}^2\text{g}^{-1}$); thus, when they bound to the interface, there was only a small amount of particle surface area that encroached into the lamellae of the foam. This translates to a lower effective volume fraction occupied by spherical particles within the lamellae, which affects the stability of the liquid film against drainage. As a result, the spherical colloidal particles were unable to interact with much of the water in the lamellae outside of their protruded surface area, and thus liquid drainage occurred for the unhindered water, which caused the increase in the reduced osmotic pressure of the system. The fumed particles possessed much higher surface areas (i.e. $\sim 195 \pm 20 \text{ m}^2\text{g}^{-1}$); and therefore, can take up larger areas on the interface and provide more interaction with the continuous phase in the lamella to sterically hinder the gravity-induced drainage, leading to the plateaus shown in figure 5(c). Therefore, while the spherical colloidal and fumed particles make similar amounts of long-lasting foam, they resist liquid drainage to a different degree and possess different foam quality throughout the foam column.

3.3. Microstructure

Imaging the bubble microstructure can be an invaluable tool that allows for in-depth analysis of the foam to investigate how the bubble shape and size, and the foam destabilization mechanisms can be impacted by various particle attributes. The microstructure images for foams stabilized with the SDS surfactant and fumed and spherical silica particles are provided in figure 6 at varying times from 60 s to 3600 s after the foam generation. Starting with SDS, it can be seen that destabilization happened continuously over the hour, from $12\,971 \pm 1\,430$ bubbles at 60 s to 118 ± 21 bubbles at 3600 s. The foam lamellas also visually decreased in size which corroborates the increase in the reduced osmotic pressure over time displayed in figure 5(a). For particle-stabilized foams, the generated bubbles are much larger in size initially than those formed in the SDS foam and that there are fewer in numbers. For the case of fumed silica particles, unlike the SDSstabilized foam, the liquid drainage seems to be more prominent only at early times, in line with the osmotic pressure data in figure 5(c). The system appeared to be undergoing some bubble coarsening but was stable over the rest of the 3600 s and for at least 109 h after initial generation, at which point the trial was concluded. For the case of spherical particles, the foam appears to drain much more quickly as can be seen by the thinning of the lamellae over the hour. The Pickering foams exhibited a rough texture compared to the SDS-stabilized

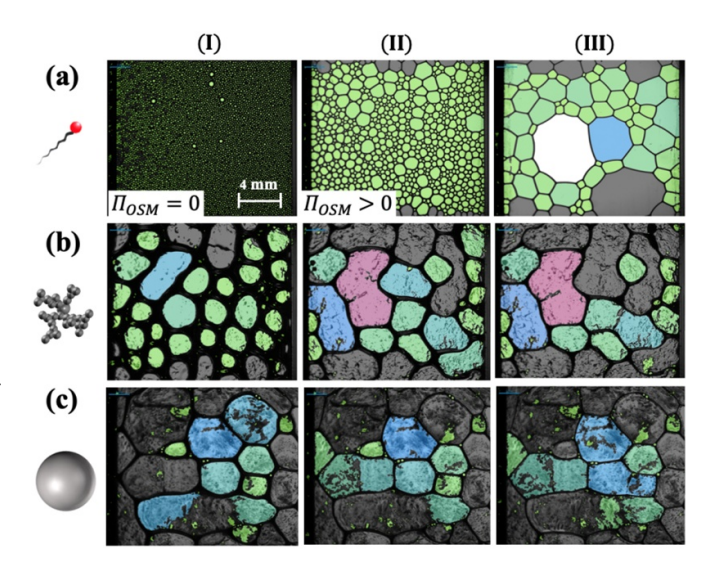


Figure 6. Comparison of microstructures captured for SDS-stabilized foam (top row) and Pickering foams stabilized by fumed silica particles (middle row) and the spherical colloidal silica particles (bottom row). Microstructure is captured as a function of time; from left to right displaying the foam at (I) 60, (II) 600, (III) 3 600 s, respectively.

foams, due to the shell of particles that encapsulated the bubbles surface and resulted in an enhanced bubble stability to coarsening.

3.4. Interfacial rheological properties - dilatation data

The dilatational rheology of particle-laden interfaces was probed for both particle types as a function of the surface pressure. Shrinking the pendant drop leads to an increase in the effective surface pressure due to an increased interparticle interactions and particle surface packing. Figures 7(a) and (b) illustrate the elastic ($\kappa^{s'}$) and viscous ($\kappa^{s''}$) dilatational moduli of the resulting microstructure. Networks created by fumed and spherical particles exhibit similar maximum elastic moduli of 162 ± 20 mN m⁻¹ and 171 ± 22 mN m⁻¹, with a negligible loss modulus in both cases. However, the extent of surface area changes that can be imposed onto the particle-laden interface, while the network upholds this high magnitude of $\kappa^{s'}$, was different between the two particle types. While the spherical colloidal particles had a narrow window of surface pressures over which the network exhibited its largest elastic modulus, the fumed particles sustained a large value of $\kappa^{s'}$ over a broader range of surface pressures; the fumed particle network was able to maintain a strong resistance to the interfacial deformation as the surface area decreased.

The dilational rheology data can be used to assess the Gibbs elasticity criterion in relation with the stability of foams [31, 94, 95]. This criterion states that if the dilatational modulus of the bubble surface (κ^s) is greater than $\frac{\gamma_{\rm eff}}{2}$, with $\gamma_{\rm eff}$ being the effective surface tension in presence of the stabilizer, the resultant bubble would be stable against Ostwald ripening. This result stems from the overall change in the Laplace pressure of the system in the process of bubble shrinkage as follows.

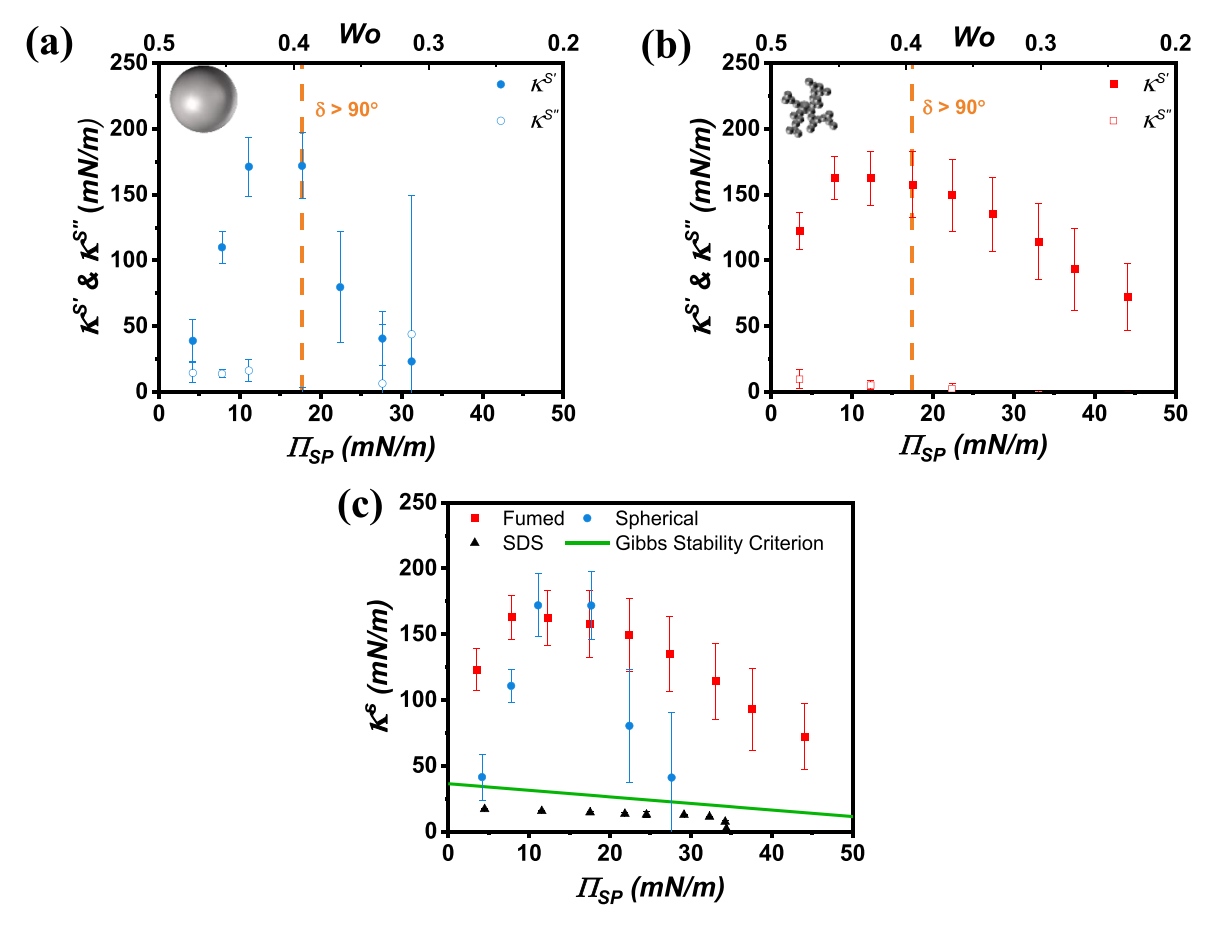


Figure 7. Dilational surface elastic $(\kappa^{s'})$ and viscous $(\kappa^{s''})$ moduli for interfacial networks of (a) spherical and (b) fumed silica particles as a function of surface pressure. The Worthington number corresponding to the measurement at each surface pressure is provided on the figure. The vertical dashed lines represent the surface pressure beyond which the phase angle is larger than 90°; (c) comparison of the dilatational modulus (κ^s) data for the air-water interface in presence of fumed particles (red squares), spherical particles (blue circles), and SDS molecules (black triangles) as a function of the surface pressure; the solid line represents the Gibbs stability criterion $\kappa^s > \frac{\gamma_{eff}}{2}$.

The pressure-drop (ΔP) across the surface of a bubble, with radius R, can be captured using the Young–Laplace equation:

$$\Delta P = P_{\rm in} - P_{\rm ext} = \frac{2\gamma_{\rm eff}}{R}.$$
 (7a)

The change in the Laplace pressure that will result from a change in the bubble size, due to Oswald ripening, can be captured as:

$$\frac{\mathrm{d}\Delta P}{\mathrm{d}R} = -\frac{2\gamma_{\mathrm{eff}}}{R^2} + \frac{2}{R}\frac{\delta\gamma_{\mathrm{eff}}}{\delta R}.\tag{7b}$$

In order to incorporate the effect of stabilizers, present on the surface, the definition of surface dilatational modulus can be written out as follows:

$$K^{s} = \left(\frac{\delta \gamma_{\text{eff}}}{\delta \ln A}\right)_{T} = A \left(\frac{\delta \gamma_{\text{eff}}}{\delta A}\right)_{T} = \frac{R}{2} \left(\frac{\delta \gamma_{\text{eff}}}{\delta R}\right)_{T}.$$
 (7c)

Combining equations (7b, c) yields:

$$\frac{\mathrm{d}\Delta P}{\mathrm{d}R} = -\frac{2\gamma_{\mathrm{eff}}}{R^2} + \frac{4\kappa^s}{R^2} > 0 \text{ for } \kappa^s > \frac{\gamma_{\mathrm{eff}}}{2}.$$
 (7d)

Using the dilational rheology data, the surface modulus of the network obtained at different surface pressures can be compared to the value of $\frac{\gamma_{\text{eff}}}{2}$, at that surface pressure, as shown in figure 7(c). For comparison, data obtained for SDS-laden air-water interface is also provided on the same plot [96]. Results illustrated in figure 7(c) confirm that the Gibbs elasticity criterion is satisfied for the particle-laden surfaces by both particle types over the range of surface pressures studied, which is in line with the stable bubbles formed in the Pickering foam samples that retained their size with time (see figure 6). In contrast, such mechanical robustness is lacking in SDS-laden monolayers, which is in agreement with the bubble coarsening that persisted in the SDS-stabilized foams. For both particle types, the particle-laden interface exhibited a frequency-independent elastic response in the dilatation mode (see supporting information, figure S3). The mathematical derivation of the long-term bubble stability criterion for a system at thermodynamic equilibrium (i.e., at local thermal, chemical potential, and mechanical equilibrium) that allows for gas transport across the bubble surfaces can be found in the recent work of Vermant and coworkers on Ultrastable Micrometer-Sized Foams [97].

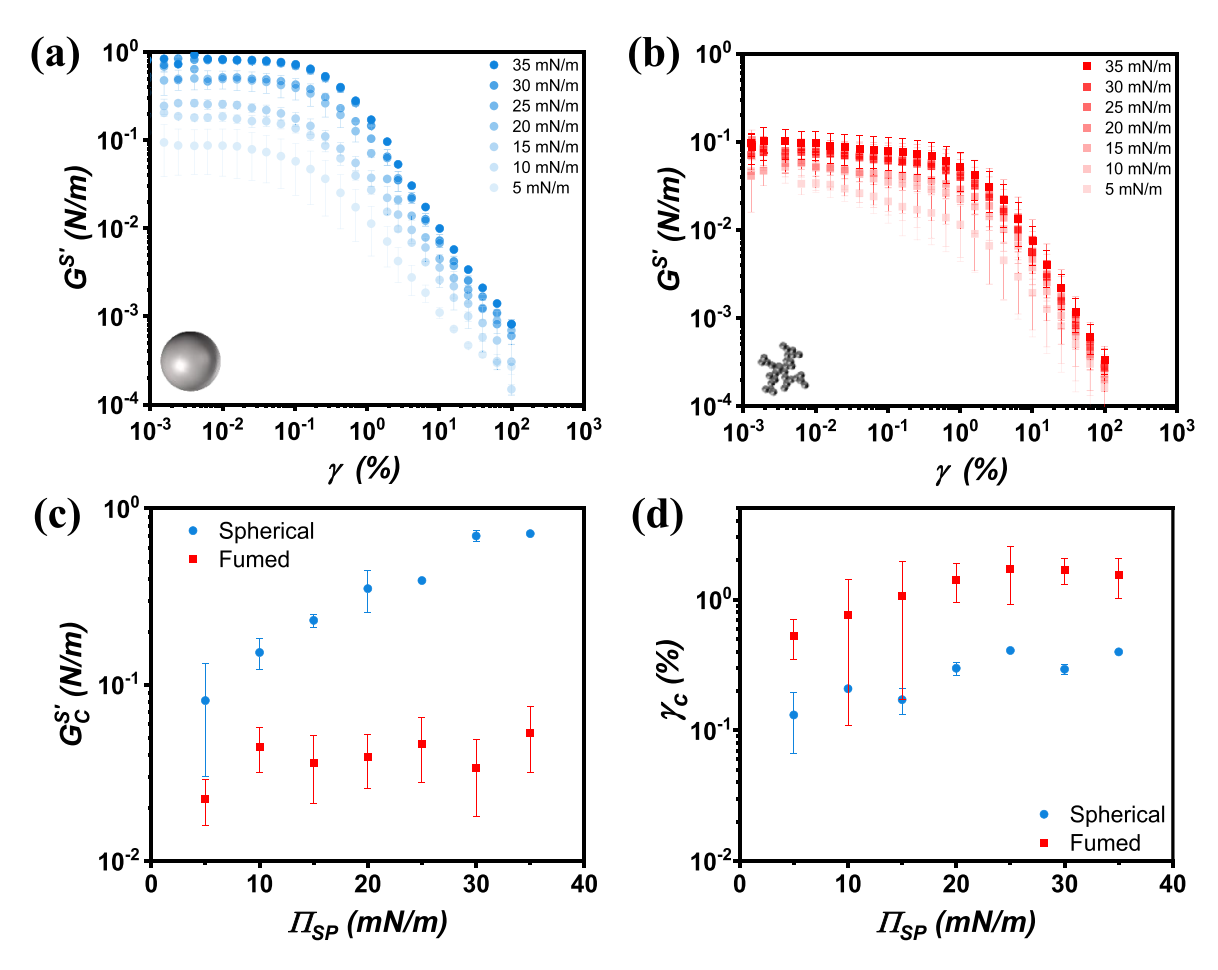


Figure 8. Amplitude sweeps for interfacial networks formed by (a) spherical and (b) fumed silica particles as a function of the monolayer surface pressure; (c) critical elastic modulus at yield, and (d) critical strain of the interfacial networks as a function of the surface pressure for both networks formed by the spherical and fumed particles.

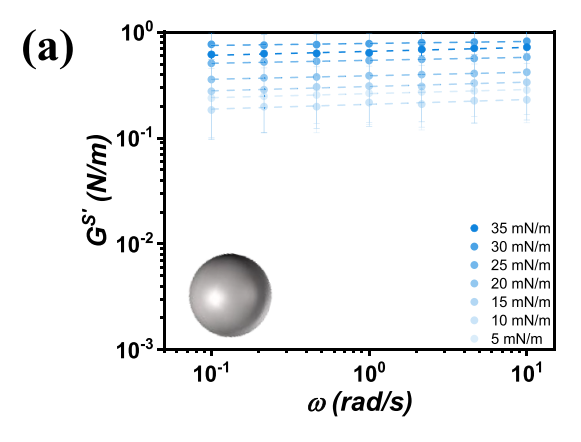
3.5. Interfacial rheological properties - shear data

Utilizing the DWR setup along with a ribbon trough and a Wilhelmy plate, the shear elastic $(G^{s'})$ and viscous $(G^{s''})$ moduli were gathered for both networks formed by the spherical and fumed silica particles at the air—water interface. Amplitude sweeps were conducted to identify the range of shear strains corresponding to the LVR for both samples, results of which are shown in figures 8(a) and (b). As the interface was compressed to attain larger surface pressures, an increase in the elastic modulus was obtained for both particle types. However, the values of surface elastic modulus for the fumed particle networks were about one order of magnitude lower than that of the interfacial films formed by the spherical particles, which could be resulting from the difference in the structure of the particles that make up the network in each case.

The critical shear strain (γ_c) , beyond which the interfacial network is destroyed, was also determined by capturing the transition from a plateau value in the shear elastic modulus $(G_c^{s\prime})$ to its sharp decrease with an increase in the applied shear strain. The critical shear properties obtained via the crossover of the linear and non-linear trendlines are shown in figures 8(c) and (d). The critical strain γ_c increased for both fumed and spherical colloidal particle networks by increasing the surface

pressure; the networks exhibiting higher surface pressures sustained a larger strain prior to microstructure breakup. In addition, the critical shear strain was higher for the network formed by the fumed silica particles in comparison to the microstructure created by the spherical particles. This behavior could be attributed to the more amorphous nature of the fumed silica particles, which could allow them to rearrange the chains at the interface under increased strain and entwine with other particles due to their flexible chains of primary silica particles. Using the information obtained from the amplitude sweep measurements, the yield stress of each network can be estimated as $\tau_Y = \gamma_c G_c^{s}$, which defines the stress necessary to break the solid network and cause the surface to flow. The magnitude of yield stress for each network at various surface pressures are provided in the supporting information (see figure S4).

Once the linear viscoelastic (LVE) regime was located for both particle samples, a shear strain amplitude within the associated LVE range was utilized to perform the frequency sweep experiments. These frequency trials were used to gather information on how the shear elastic and viscous moduli change with the frequency of oscillations, at different surface pressures. The elastic surface shear modulus results are provided in figure 9 and data on the frequency dependence of the viscous modulus are provided in the supporting



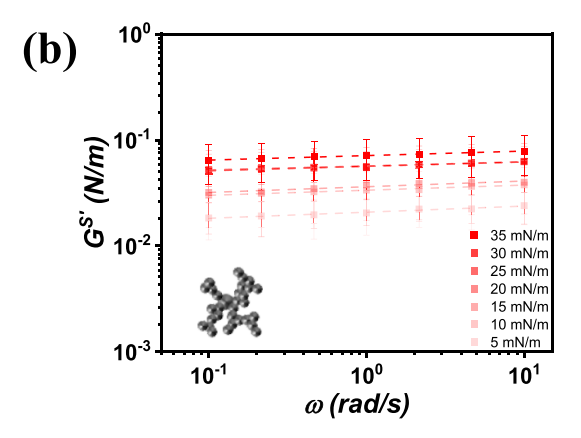


Figure 9. Surface shear elastic response $(G^{s'})$ of interfacial films at various surface pressures probed using a shear strain of 0.05% and over a frequency range of 0.1–10 rad s⁻¹ for (a) spherical and (b) fumed silica particle networks.

information. In line with the findings obtained from the amplitude sweep experiments, the network formed by the spherical colloidal particles exhibited a surface shear elastic modulus which was an order of magnitude larger than that obtained for the fumed silica particle network. To further analyze the dependence of the surface shear elastic modulus $(G^{s'})$ on the frequency (ω) of oscillations, power law trendlines ($G^{s'} \propto$ ω^{B}) were plotted and the exponents were compared. It has been shown that when the exponent approaches 1, i.e., B =1, the network is viscous dominated, whereas for exponent approaching 0, the network is more solid-like and the response is elastic dominated [74]. The exponents obtained for the fumed particle networks were initially ~0.06 and decreased with increasing surface pressure to ~ 0.04 , for the largest surface pressure analyzed, while for the spherical colloidal particles the exponent remained ~ 0.04 with increasing the surface pressure. These findings indicate that both interfaces were firmly solid-like. Similar analysis was carried out on the surface viscous modulus results of which are provided in the supporting information (see figure S5).

4. Conclusions

This work investigated the impact of particle roughness (fumed vs. spherical colloidal silica particles) on interfacial rheological properties of networks formed at the air-water interface and their relationship to the stability of Pickering foams. Foam stability, characterized by microstructure and liquid content over time, was compared between particlestabilized foams and foams stabilized by the common foaming agent SDS. Both particle systems exhibited increased foam stability, evidenced by longer foam half-lives and reduced bubble coarsening compared to SDS-stabilized foams. This stability was attributed to the mechanical robustness of the interfacial networks formed by particles, which protected the bubbles from coarsening. The dilational surface modulus of the particle-laden networks met the Gibbs elasticity criterion, while SDS-stabilized foams lacked such robustness. The resistance to liquid drainage differed between the particle systems, with fumed silica particle-stabilized foams demonstrating greater resistance. This resistance was linked to the larger surface area of fumed particles and their enhanced interaction with water within the foam lamellae, as well as the rheological properties of the particle-laden interface. The fumed particles exhibited a broader range of surface pressures for maintaining resistance and a higher critical shear strain before yielding, contributing to their enhanced stability against liquid drainage. Both particle types created elastic networks at the air-water interface, stabilizing the foams and increasing their half-life compared to SDS-stabilized systems. However, the degree to which different destabilization mechanisms were prevented or arrested could depend on particle attributes and interfacial rheological properties. This study establishes connections between interface rheology and macroscopic foam characteristics, providing a framework for engineering interfacial systems with desired properties.

Data availability statement

All data that support the findings of this study are included within the article (and any supplementary files).

Acknowledgments

We would like to thank the National Science Foundation (NSF CAREER CBET—2144020) as well as the ACS-PRF (61617—DNI9) for providing funding for this project.

ORCID iD

Sepideh Razavi https://orcid.org/0000-0003-1225-6081

References

- [1] Matis K A and Mavros P 1991 Foam/froth flotation Sep. Purif. Methods 20 163–98
- [2] McCoy T M, Parks H C W and Tabor R F 2018 Highly efficient recovery of graphene oxide by froth flotation using a common surfactant Carbon 135 164–70
- [3] Yoon I-H, Kim S E, Choi M, Kim S, Choi W-K and Jung C-H 2020 Highly enhanced foams for stability and

- decontamination efficiency with a fluorosurfactant, silica nanoparticles, and Ce(IV) in radiological application *Environ. Technol. Innov.* **18** 100744
- [4] Lambert D P, Nikolov A D, Wasan D T, Williams M S, Howe A M and Woodham W H 2021 A novel defoamer for processing nuclear waste: testing and performance *Environ*. *Prog. Sustain. Energy* 40 e13607
- [5] Ferreira F V, Otoni C G, De France K J, Barud H S, Lona L M F, Cranston E D and Rojas O J 2020 Porous nanocellulose gels and foams: breakthrough status in the development of scaffolds for tissue engineering *Mater*. *Today* 37 126–41
- [6] Chen L, Zhou X and He C 2019 Mesoporous silica nanoparticles for tissue-engineering applications Wiley Interdiscip. Rev.- Nanomed. Nanobiotechnol. 11 e1573
- [7] Kim M Y and Kim J 2017 Chitosan microgels embedded with catalase nanozyme-loaded mesocellular silica foam for glucose-responsive drug delivery ACS Biomater. Sci. Eng. 3 572–8
- [8] Etemad S, Kantzas A and Bryant S 2020 Experimental investigation of CO₂ foam stability enhancement by partitioning particles J. Pet. Sci. Eng. 194 107540
- [9] Yu H, Zhu Y F, Hui A P, Yang F F and Wang A Q 2021 Removal of antibiotics from aqueous solution by using porous adsorbent templated from eco-friendly Pickering aqueous foams J. Environ. Sci. 102 352–62
- [10] Calhoun S G K, Chandran Suja V and Fuller G G 2022 Foaming and antifoaming in non-aqueous liquids Curr. Opin Colloid Interface Sci. 57 101558
- [11] Amirsadat S A, Moradi B, Hezave A Z, Najimi S and Farsangi M H 2017 Investigating the effect of nano-silica on efficiency of the foam in enhanced oil recovery *Korean J. Chem. Eng.* 34 3119–24
- [12] Lu T, Li Z and Zhou Y 2017 Flow behavior and displacement mechanisms of nanoparticle stabilized foam flooding for enhanced heavy oil recovery *Energies* 10 560
- [13] Liu S, Yuan F, Sang M, Zhou J, Zhang J, Wang S, Li J, Xuan S and Gong X 2021 Functional sponge-based triboelectric nanogenerators with energy harvesting, oil–water separating and multi-mode sensing performance *J. Mater. Chem.* A 9 6913–23
- [14] Wanniarachchi W A M, Ranjith P G, Perera M S A, Lashin A, Al Arifi N and Li J C 2015 Current opinions on foam-based hydro-fracturing in deep geological reservoirs *Geomech*. *Geophys. Geo-Energy Geo-Resour.* 1 121–34
- [15] Hematpur H, Mahmood S M, Nasr N H and Elraies K A 2018 Foam flow in porous media: concepts, models and challenges J. Nat. Gas Sci. Eng. 53 163–80
- [16] Zhou H, Qu C, Lu G, Li Z, Wang X, Yin H and Feng Y 2021 Deliquification of low-productivity natural gas wells with in situ generated foams and heat Energy Fuels 35 9873–82
- [17] Britan A, Liverts M, Ben-Dor G, Koehler S A and Bennani N 2009 The effect of fine particles on the drainage and coarsening of foam *Colloids Surf.* A 344 15–23
- [18] Pawar A B, Caggioni M, Ergun R, Hartel R W and Spicer P T 2011 Arrested coalescence in Pickering emulsions Soft Matter 7 7710-6
- [19] Beltramo P J, Gupta M, Alicke A, Liascukiene I, Gunes D Z, Baroud C N and Vermant J 2017 Arresting dissolution by interfacial rheology design *Proc. Natl Acad. Sci.* 114 10373–8
- [20] Princen H M and Kiss A D 1987 Osmotic pressure of foams and highly concentrated emulsions. 2. Determination from the variation in volume fraction with height in an equilibrated column *Langmuir* 3 36–41
- [21] Stocco A, Drenckhan W, Rio E, Langevin D and Binks B P 2009 Particle-stabilised foams: an interfacial study Soft Matter 5 2215–22

- [22] Oetjen K, Bilke-Krause C, Madani M and Willers T 2014 Temperature effect on foamability, foam stability, and foam structure of milk *Colloids Surf.* A 460 280-5
- [23] Yang L L, Wang T D, Yang X, Jiang G C, Luckham P F, Xu J P, Li X L and Ni X X 2019 Highly stabilized foam by adding amphiphilic Janus particles for drilling a high-temperature and high-calcium geothermal well *Ind. Eng. Chem. Res.* 58 9795–805
- [24] Katepalli H, John V T, Tripathi A and Bose A 2017 Microstructure and rheology of particle stabilized emulsions: effects of particle shape and inter-particle interactions J. Colloid Interface Sci. 485 11–17
- [25] Alzobaidi S, Lotfollahi M, Kim I, Johnston K P and DiCarlo D A 2017 Carbon dioxide-in-brine foams at high temperatures and extreme salinities stabilized with silica nanoparticles *Energy Fuels* 31 10680–90
- [26] Yilixiati S, Rafiq R, Zhang Y and Sharma V 2018 Influence of Salt on Supramolecular Oscillatory Structural Forces and Stratification in Micellar Freestanding Film ACS Nano 12, 1050-61
- [27] Khajehpour M, Reza Etminan S, Goldman J, Wassmuth F and Bryant S 2018 Nanoparticles as foam stabilizer for steam-foam process SPE J. 23 2232–42
- [28] Tengku Mohd T A, Noor Fitrah A B, Awang N and Talib A 2018 Aqueous foams stabilized with silica nanoparticle and alpha olefin sulfonates surfactant *J. Mech. Eng. Sci.* 12 3759–70
- [29] Ochoa C, Xu C, Martínez Narváez C D V, Yang W, Zhang Y and Sharma V 2021 Drainage via stratification and nanoscopic thickness transitions of aqueous sodium naphthenate foam films Soft Matter 17 8915–24
- [30] Yao X, Zhao G, Dai C, Wu Y and Lyu Y 2020 Interfacial characteristics and the stability mechanism of a dispersed particle gel (DPG) three-phase foam *J. Mol. Liq.* 301 112425
- [31] Cervantes Martinez A, Rio E, Delon G, Saint-Jalmes A, Langevin D and Binks B P 2008 On the origin of the remarkable stability of aqueous foams stabilised by nanoparticles: link with microscopic surface properties *Soft Matter* 4 1531–5
- [32] Tyowua A T and Binks B P 2020 Growing a particle-stabilized aqueous foam J. Colloid Interface Sci. 561 127–35
- [33] Hurtado Y, Franco Ariza C, Riazi M and Cortés F 2019 Improving the stability of nitrogen foams using silica nanoparticles coated with polyethylene glycol *J. Mol. Liq.* 300 112256
- [34] Vishal B and Ghosh P 2019 The effect of silica nanoparticles on the stability of aqueous foams *J. Disperse Sci. Technol.* **40** 206–18
- [35] Denkov N, Tcholakova S and Politova-Brinkova N 2020 Physicochemical control of foam properties Curr. Opin Colloid Interface Sci. 50 101376
- [36] Bindal S K, Sethumadhavan G, Nikolov A D and Wasan D T 2002 Foaming mechanisms in surfactant free particle suspensions AIChE J. 48 2307–14
- [37] Safouane M, Langevin D and Binks B P 2007 Effect of particle hydrophobicity on the properties of silica particle layers at the air—water interface *Langmuir* 23 11546–53
- [38] Maestro A, Guzmán E, Santini E, Ravera F, Liggieri L, Ortega F and Rubio R 2012 Wettability of silica nanoparticle-surfactant nanocomposite interfacial layers Soft Matter 8 837–43
- [39] Fu Y, Wan Z, Zhao G, Jia W and Zhao H 2021 Flexible conductive sodium alginate/chitosan foam with good mechanical properties and magnetic sensitivity Smart Mater. Struct. 30 075027
- [40] Liu Q, Qu H, Liu S, Zhang Y, Zhang S, Liu J, Peng B and Luo D 2020 Modified Fe $_3$ O4 nanoparticle used for

- stabilizing foam flooding for enhanced oil recovery *Colloids Surf.* A **605** 125383
- [41] Worthen A J, Bagaria H G, Chen Y, Bryant S L, Huh C and Johnston K P 2013 Nanoparticle-stabilized carbon dioxide-in-water foams with fine texture *J. Colloid Interface Sci.* 391 142–51
- [42] Geng D, Li J, Li H and Huang W 2021 Effects of particle combinations with different wettability on foam structure and stability Front. Mater. 8 699187
- [43] Hunter T, Pugh R, Franks G and Jameson G 2008 The role of particles in stabilising foams and emulsions Adv. Colloid Interface Sci. 137 57–81
- [44] Amani P, Miller R, Javadi A and Firouzi M 2022 Pickering foams and parameters influencing their characteristics Adv. Colloid Interface Sci. 301 102606
- [45] Hu N, Li Y, Wu Z, Lu K, Huang D and Liu W 2018 Foams stabilization by silica nanoparticle with cationic and anionic surfactants in column flotation: effects of particle size *J. Taiwan Inst. Chem. Eng.* **88** 62–69
- [46] Gmoser R, Bordes R, Nilsson G, Altskär A, Stading M, Lorén N and Berta M 2017 Effect of dispersed particles on instant coffee foam stability and rheological properties Eur. Food Res. Technol. 243 115–21
- [47] Fameau A-L, Lam S and Velev O D 2013 Multi-stimuli responsive foams combining particles and self-assembling fatty acids *Chem. Sci.* 4 3874–81
- [48] Chen X, Da C, Hatchell D C, Daigle H, Ordonez-Varela J-R, Blondeau C and Johnston K P 2023 Ultra-stable CO₂-in-water foam by generating switchable Janus nanoparticles in-situ J. Colloid Interface Sci. 630 828–43
- [49] Ozdemir O, Hampton M and Nguyen A 2011 Formation and stability of foams stabilized by fine particles with similar size, contact angle and different shapes *Colloids Surf.* A 382 132–8
- [50] Amiri A, Øye G and Sjöblom J 2009 Influence of pH, high salinity and particle concentration on stability and rheological properties of aqueous suspensions of fumed silica Colloids Surf. A 349 43–54
- [51] Gao S, Ochoa C, Sharma V and Srivastava S 2022 Salt weakens intermicellar interactions and structuring in bulk solutions and foam films *Langmuir* 38 11003–14
- [52] Sun X, Chen Y and Zhao J 2016 Highly stable aqueous foams generated by fumed silica particles hydrophobised in situ with a quaternary ammonium Gemini surfactant RSC Adv. 6 38913–8
- [53] Shojaei M J, Méheust Y, Osman A, Grassia P and Shokri N 2021 Combined effects of nanoparticles and surfactants upon foam stability *Chem. Eng. Sci.* 238 116601
- [54] Da C, Chen X, Zhu J, Alzobaidi S, Garg G and Johnston K P 2022 Elastic gas/water interface for highly stable foams with modified anionic silica nanoparticles and a like-charged surfactant *J. Colloid Interface Sci.* 608 1401–13
- [55] Zhu J, Yang Z, Li X, Hou L and Xie S 2019 Experimental study on the microscopic characteristics of foams stabilized by viscoelastic surfactant and nanoparticles *Colloids Surf.* A 572 88–96
- [56] Pang B, Zhang H, Schilling M, Liu H, Wang X, Rehfeldt F and Zhang K 2020 High-internal-phase Pickering emulsions stabilized by polymeric dialdehyde cellulose-based nanoparticles ACS Sustain. Chem. Eng. 8 7371–9
- [57] Sheng Y, Lin K, Binks B P and Ngai T 2020 Ultra-stable aqueous foams induced by interfacial co-assembly of highly hydrophobic particles and hydrophilic polymer *J. Colloid Interface Sci.* 579 628–36
- [58] Worthen A J, Bryant S L, Huh C and Johnston K P 2013 Carbon dioxide-in-water foams stabilized with nanoparticles and surfactant acting in synergy AIChE J. 59 3490–501

- [59] Andrieux S, Quell A, Stubenrauch C and Drenckhan W 2018 Liquid foam templating—a route to tailor-made polymer foams Adv. Colloid Interface Sci. 256 276–90
- [60] Lee J, Nikolov A and Wasan D 2013 Stability of aqueous foams in the presence of oil: on the importance of dispersed vs solubilized oil *Ind. Eng. Chem. Res.* 52 66–72
- [61] Zheng B, Zheng B, Carr A J, Yu X, McClements D J and Bhatia S R 2020 Emulsions stabilized by inorganic nanoclays and surfactants: stability, viscosity, and implications for applications *Inorganica Chim. Acta* 508 119566
- [62] Kostakis T, Ettelaie R and Murray B S 2006 Effect of high salt concentrations on the stabilization of bubbles by silica particles *Langmuir* 22 1273–80
- [63] Manga M S, Hunter T N, Cayre O J, York D W, Reichert M D, Anna S L, Walker L M, Williams R A and Biggs S R 2016 Measurements of submicron particle adsorption and particle film elasticity at oil–water interfaces *Langmuir* 32 4125–33
- [64] Wasan D T, Nikolov A D, Lobo L A, Koczo K and Edwards D A 1992 Foams, thin films and surface rheological properties *Prog. Surf. Sci.* 39 119–54
- [65] Xu W, Nikolov A, Wasan D T, Gonsalves A and Borwankar R P 2003 Foam film rheology and thickness stability of foam-based food products *Colloids Surf. A* 214 13–21
- [66] van den Berg M E H, Kuster S, Windhab E J, Sagis L M C and Fischer P 2018 Nonlinear shear and dilatational rheology of viscoelastic interfacial layers of cellulose nanocrystals *Phys. Fluids* 30 072103
- [67] Nguyen T X D, Razavi S and Papavassiliou D V 2022 Janus nanoparticle and surfactant effects on oil drop migration in water under shear J. Phys. Chem. B 126 6314–23
- [68] Van Hooghten R, Blair V E, Vananroye A, Schofield A B, Vermant J and Thijssen J H J 2017 Interfacial rheology of sterically stabilized colloids at liquid interfaces and its effect on the stability of Pickering emulsions *Langmuir* 33 4107–18
- [69] Vu T V, Razavi S and Papavassiliou D V 2022 Effect of Janus particles and non-ionic surfactants on the collapse of the oil-water interface under compression *J. Colloid Interface* Sci. 609 158–69
- [70] Razavi S, Lin B, Lee K Y C, Tu R S and Kretzschmar I 2019 Impact of surface amphiphilicity on the interfacial behavior of Janus particle layers under compression *Langmuir* 35 15813–24
- [71] Razavi S, Hernandez L M, Read A, Vargas W L and Kretzschmar I 2020 Surface tension anomaly observed for chemically-modified Janus particles at the air/water interface J. Colloid Interface Sci. 558 95–99
- [72] Derkach S, Krägel J and Miller R 2009 Methods of measuring rheological properties of interfacial layers (experimental methods of 2D rheology) *Colloid J.* **71** 1–17
- [73] Pitois O and Rouyer F 2019 Rheology of particulate rafts, films, and foams Curr. Opin Colloid Interface Sci. 43 125–37
- [74] Yu K, Zhang H, Biggs S, Xu Z, Cayre O J and Harbottle D 2018 The rheology of polyvinylpyrrolidone-coated silica nanoparticles positioned at an air-aqueous interface *J. Colloid Interface Sci.* 527 346–55
- [75] Correia E L, Winter H H and Razavi S 2023 Two-dimensional glass transition–like behavior of Janus particle–laden interface *Rheol. Acta* 62 239–51
- [76] Alzobaidi S, Da C, Wu P, Zhang X, Rabat-Torki N J, Harris J M, Hackbarth J E, Lu C, Hu D and Johnston K P 2021 Tuning nanoparticle surface chemistry and interfacial properties for highly stable nitrogen-in-brine foams *Langmuir* 37 5408–23
- [77] Benjamins J and Lucassen-Reynders E H 1998 Surface dilational rheology of proteins adsorbed at air/water and

- oil/water interfaces *Studies in Interface Science* vol 7, ed D Möbius and R Miller (Amsterdam: Elsevier) pp 341–84
- [78] Zhu J, Da C, Chen J and Johnston K P 2022 Ultrastable N₂/water foams stabilized by dilute nanoparticles and a surfactant at high salinity and high pressure *Langmuir* 38 5392–403
- [79] Thijssen J H J and Vermant J 2018 Interfacial rheology of model particles at liquid interfaces and its relation to (bicontinuous) Pickering emulsions J. Phys.: Condens. Matter 30 023002
- [80] Correia E L, Brown N and Razavi S 2021 Janus particles at fluid interfaces: stability and interfacial rheology *Nanomaterials* 11 374
- [81] Razavi S, Cao K D, Lin B, Lee K Y C, Tu R S and Kretzschmar I 2015 Collapse of particle-laden interfaces under compression: buckling vs particle expulsion *Langmuir* 31 7764–75
- [82] Prevo B G and Velev O D 2004 Controlled, rapid deposition of structured coatings from micro- and nanoparticle suspensions *Langmuir* 20 2099–107
- [83] Arzt E, Quan H, McMeeking R M and Hensel R 2021 Functional surface microstructures inspired by nature—from adhesion and wetting principles to sustainable new devices *Prog. Mater. Sci.* 120 100823
- [84] Feitosa K, Marze S, Saint-Jalmes A and Durian D 2005 Electrical conductivity of dispersions: from dry foams to dilute suspensions *J. Phys.: Condens. Matter* 17 6301
- [85] Cohen-Addad S and Höhler R 2014 Rheology of foams and highly concentrated emulsions Curr. Opin Colloid Interface Sci. 19 536–48
- [86] Maestro A, Drenckhan W, Rio E and Höhler R 2013 Liquid dispersions under gravity: volume fraction profile and osmotic pressure Soft Matter 9 2531–40

- [87] Forel E, Rio E, Schneider M, Beguin S, Weaire D, Hutzler S and Drenckhan W 2016 The surface tells it all: relationship between volume and surface fraction of liquid dispersions Soft Matter 12 8025–9
- [88] Berry J D, Neeson M J, Dagastine R R, Chan D Y C and Tabor R F 2015 Measurement of surface and interfacial tension using pendant drop tensiometry *J. Colloid Interface* Sci. 454 226–37
- [89] Da C, Zhang X, Alzobaidi S, Hu D, Wu P and Johnston K P 2021 Tuning surface chemistry and ionic strength to control nanoparticle adsorption and elastic dilational modulus at air-brine interface *Langmuir* 37 5795–809
- [90] Hermans E and Vermant J 2014 Interfacial shear rheology of DPPC under physiologically relevant conditions Soft Matter 10 175–86
- [91] Vandebril S, Franck A, Fuller G G, Moldenaers P and Vermant J 2010 A double wall-ring geometry for interfacial shear rheometry *Rheol. Acta* 49 131–44
- [92] Binks B P 2002 Particles as surfactants—similarities and differences Curr. Opin Colloid Interface Sci. 7 21–41
- [93] Stone H A, Koehler S A, Hilgenfeldt S and Durand M 2003 Perspectives on foam drainage and the influence of interfacial rheology J. Phys.: Condens. Matter 15 S283
- [94] Gibbs J W 1993 The Scientific Papers of J. Willard Gibbs vol 1 (Woodbridge: Ox Bow)
- [95] Maestro A, Rio E, Drenckhan W, Langevin D and Salonen A 2014 Foams stabilised by mixtures of nanoparticles and oppositely charged surfactants: relationship between bubble shrinkage and foam coarsening Soft Matter 10 6975–83
- [96] Correia E L, Brown N, Ervin A, Papavassiliou D V and Razavi S 2022 Contamination in sodium dodecyl sulfate solutions: insights from the measurements of surface tension and surface rheology *Langmuir* 38 7179–89
- [97] Hakim M R, Oblak L and Vermant J Facile and Robust Production of Ultrastable Micrometer-Sized Foams ACS Eng. Au 3c00005